



The TW Hya Rosetta Stone Project. II. Spatially Resolved Emission of Formaldehyde Hints at Low-temperature Gas-phase Formation

Jeroen Terwisscha van Scheltinga^{1,2} , Michiel R. Hogerheijde^{2,3} , L. Ilesdore Cleeves⁴ , Ryan A. Loomis⁵ , Catherine Walsh⁶ , Karin I. Öberg⁷ , Edwin A. Bergin⁸ , Jennifer B. Bergner⁹ , Geoffrey A. Blake^{10,11} , Jenny K. Calahan⁸ , Paolo Cazzoletti² , Ewine F. van Dishoeck^{2,12} , Viviana V. Guzmán¹³ , Jane Huang^{7,8,16} , Mihkel Kama^{14,15} , Chunhua Qi⁷ , Richard Teague⁷ , and David J. Wilner⁷

¹ Laboratory for Astrophysics, Leiden Observatory, Leiden University, P.O. Box 9513, 2300 RA Leiden, The Netherlands; jeroentvs@strw.leidenuniv.nl

² Leiden Observatory, Leiden University, P.O. Box 9513, 2300 RA Leiden, The Netherlands

³ Anton Pannekoek Institute for Astronomy, University of Amsterdam, Science Park 904, 1098 XH, Amsterdam, The Netherlands

⁴ Astronomy Department, University of Virginia, Charlottesville, VA 22904, USA

⁵ National Radio Astronomy Observatory, 520 Edgemont Road, Charlottesville, VA 22903, USA

⁶ School of Physics and Astronomy, University of Leeds, Leeds LS2 9JT, UK

⁷ Center for Astrophysics | Harvard & Smithsonian, 60 Garden Street, Cambridge, MA 02138, USA

⁸ Department of Astronomy, University of Michigan, 1085 South University Avenue, Ann Arbor, MI 48109, USA

⁹ University of Chicago, Department of the Geophysical Sciences, Chicago, IL 60637, USA

¹⁰ Division of Chemistry & Chemical Engineering, California Institute of Technology, Pasadena, CA 91125, USA

¹¹ Division of Geological & Planetary Sciences, California Institute of Technology, Pasadena, CA 91125, USA

¹² Max-Planck-Institut für Extraterrestrische Physik, Giessenbachstraße 1, D-85748 Garching bei München, Germany

¹³ Instituto de Astronomía, Pontificia Universidad Católica de Chile, Av. Vicuña Mackenna 4860, 7820436 Macul, Santiago, Chile

¹⁴ Department of Physics and Astronomy, University College London, Gower Street, London, WC1E 6BT, UK

¹⁵ Tartu Observatory, University of Tartu, 61602 Tõravere, Estonia

Received 2020 August 28; revised 2020 October 23; accepted 2020 November 10; published 2021 January 14

Abstract

Formaldehyde (H_2CO) is an important precursor to organics like methanol (CH_3OH). It is important to understand the conditions that produce H_2CO and prebiotic molecules during star and planet formation. H_2CO possesses both gas-phase and solid-state formation pathways, involving either UV-produced radical precursors or CO ice and cold ($\lesssim 20$ K) dust grains. To understand which pathway dominates, gaseous H_2CO 's ortho-to-para ratio (OPR) has been used as a probe, with a value of 3 indicating “warm” conditions and < 3 linked to cold formation in the solid state. We present spatially resolved Atacama Large Millimeter/submillimeter Array observations of multiple ortho- and para- H_2CO transitions in the TW Hya protoplanetary disk to test H_2CO formation theories during planet formation. We find disk-averaged rotational temperatures and column densities of 33 ± 2 K, $(1.1 \pm 0.1) \times 10^{12} \text{ cm}^{-2}$ and 25 ± 2 K, $(4.4 \pm 0.3) \times 10^{11} \text{ cm}^{-2}$ for ortho- and para- H_2CO , respectively, and an OPR of 2.49 ± 0.23 . A radially resolved analysis shows that the observed H_2CO emits mostly at rotational temperatures of 30–40 K, corresponding to a layer with $z/R \geq 0.25$. The OPR is consistent with 3 within 60 au, the extent of the pebble disk, and decreases beyond 60 au to 2.0 ± 0.5 . The latter corresponds to a spin temperature of 12 K, well below the rotational temperature. The combination of relatively uniform emitting conditions, a radial gradient in the OPR, and recent laboratory experiments and theory on OPR ratios after sublimation, led us to speculate that *gas-phase* formation is responsible for the observed H_2CO across the TW Hya disk.

Unified Astronomy Thesaurus concepts: [Astrochemistry \(75\)](#); [Protoplanetary disks \(1300\)](#); [Interstellar molecules \(849\)](#); [Interstellar abundances \(832\)](#)

1. Introduction

The incorporation of complex organic molecules (COMs) into forming planets is essential to solving the puzzle of life’s origins (e.g., Herbst & van Dishoeck 2009). The answer to how and where prebiotic molecules are formed is an important step in this investigation, and starts with the study of the chemical precursors of COMs. Even for one of the simplest COMs, methanol (CH_3OH), the origin of its precursor molecule formaldehyde (H_2CO) has yet to be fully constrained in protoplanetary disks (Loomis et al. 2015; Öberg et al. 2017). Specifically, H_2CO presents a challenge in that it can potentially form via reactions in the gas phase and via formation in the ice mantles of cold grains, followed by nonthermal desorption or sublimation (Qi et al. 2013; Loomis et al. 2015; Öberg et al. 2017). The relative occurrence of both paths is important, because they take place in different

environments and thus contribute differently to the formation of methanol and other COMs. Furthermore, an unsolved question is whether the observed organic reservoir is close enough to the midplane where planets form.

Solid-state formation of H_2CO starts with the hydrogenation of CO; further hydrogenation, though with a small barrier of 400–500 K, leads to efficient formation of CH_3OH (Hiraoka et al. 1994, 2002; Watanabe & Kouchi 2002; Hidaka et al. 2004; Watanabe et al. 2004; Fuchs et al. 2009). From CH_3OH , a complex and varied chemistry can be seeded by the subsequent formation of simple sugars and sugar alcohols like glycerol, an important building block for cell membranes (Chuang et al. 2017; Fedoseev et al. 2017). In contrast, gas-phase formation of H_2CO occurs most efficiently through the reaction between atomic oxygen and methyl radicals (CH_3) (Fockenberg & Preses 2002; Atkinson et al. 2006) as well as CH_2 and hydroxyl radicals (OH). Therefore, the gas-phase formation pathway is particularly efficient where these radicals can be generated,

¹⁶ NHFP Sagan Fellow.

primarily in the UV-irradiated surface where there is efficient photodesorption and photodissociation (Aikawa et al. 2002; Loomis et al. 2015).

The first protoplanetary disks in which H_2CO was detected are those around DM Tau and GG Tau (Dutrey et al. 1997). These detections were followed by the detection of H_2CO in LkCa 15 (Aikawa et al. 2003; Thi et al. 2004). Although groundbreaking, the detections were only in the best case marginally spatially resolved and comparison to models (e.g., van Zadelhoff et al. 2003) to disentangle the origin of H_2CO was not feasible.

Recent high-resolution observations with the Atacama Large Millimeter/submillimeter Array (ALMA) of H_2CO transitions in 20 protoplanetary disks suggest that both gas-phase and solid-state formation of formaldehyde occurs, with their relative contributions varying across different disks (van der Marel et al. 2014; Loomis et al. 2015; Carney et al. 2017; Öberg et al. 2017; Guzmán et al. 2018; Kastner et al. 2018; Podio et al. 2019; Garufi et al. 2020; Pegues et al. 2020). Parametric model fits to resolved observations of H_2CO $3_{12-2_{11}}$ and $5_{15-4_{14}}$ in the disk of T Tauri star TW Hya find both warm and cold H_2CO components in compact and extended regions, respectively (Öberg et al. 2017). These studies have demonstrated that observations of multiple transitions allow for an improved determination of the rotational temperature and column density, which provides further constraints on the radial and vertical location of the emitting molecules and their origin. For example, in the disk of the Herbig Ae star HD 163296, Guzmán et al. (2018) derived for the first time a disk-averaged column density ratio of the ortho and para isomers of H_2CO in the range 1.8–2.8 with a rotational temperature of 24 K.

As first proposed by Kahane et al. (1984), the ortho-to-para ratio (OPR) of H_2CO could additionally shed light on the formation origins of this molecule. For example, H_2CO formed in warm gas would thermalize at the statistically expected OPR of 3.0, while cold formation, such as the CO-ice hydrogenation pathways, would equilibrate the OPR to a lower value consistent with the grain temperature. The expectation is that the OPR is conserved from the moment of formation, since radiative transitions between ortho- and para- H_2CO are strictly forbidden. However, recent experimental work by Hama et al. (2018) showed that for *water*, desorption *resets* the OPR to 3.0. If this is the case for H_2CO , other explanations for the observed low H_2CO OPR values are necessary and a cold-grain formation route cannot be inferred.

The disk around TW Hya is an ideal laboratory to study the chemical origin of formaldehyde in detail. TW Hya is the closest Sun-like star surrounded by a gas-rich protoplanetary disk, with a distance of 60.1 pc (Gaia Collaboration et al. 2018). Its disk has been studied extensively, in millimeter continuum and near-infrared scattered light, in various molecules, including CO and isotopologues, and in a variety of chemical tracers (e.g., Andrews et al. 2012, 2016; Akiyama et al. 2015; Walsh et al. 2016; Öberg et al. 2017; Huang et al. 2018; Teague et al. 2018). Spatially resolved observations of two H_2CO lines, $3_{12-2_{11}}$ ($0''.45 \times 0''.45$) and $5_{15-4_{14}}$ ($0''.47 \times 0''.41$), in the TW Hya disk by Öberg et al. (2017) suggested that gas-phase formation dominates in the inner regions of the disk (<10 au), while grain-surface formation contributes beyond 15 au.

In the current paper, we use a comprehensive multiline data set, including a wider range of upper-state energies,

21–141 K, and now in both ortho- and para-spin isomers, taken with ALMA toward the TW Hya disk. These data allow us to *directly* infer the radial and vertical structure of H_2CO , without having to rely on parametric models like those used by Öberg et al. (2017). We aim to elucidate the formation of this key simple organic. Our data were obtained as part of an ALMA study (“TW Hya as a Chemical Rosetta Stone,” PI L.I. Cleeves) aimed at a deep understanding of this object’s chemistry, and by extension, of that of other gas-rich protoplanetary disks. In this paper, observations of H_2CO from this ALMA project, together with archival ALMA data, are presented and used to explore the rotational temperature, column density, and OPR of H_2CO in TW Hya. Section 2 describes the observational details and data reduction, Section 3 describes the resulting radial emission and excitation profiles, and Section 4 discusses the implications for the chemical origin of H_2CO across the TW Hya disk. Section 5 summarizes the main findings.

2. Observations and Reduction

The data presented here were obtained as part of the ALMA project “TW Hya as a chemical Rosetta stone” (2016.1.00311.S, PI Cleeves); additional, archival H_2CO data were taken from ALMA projects 2013.1.00114.S (Öberg et al. 2017) and 2016.1.00464.S. The observational details (number of antennas, baseline ranges, on-source time, and calibrators) are summarized in Table 1. All data sets were processed through the standard ALMA calibration pipeline, after which self-calibration was applied. Data from 2013.1.00114.S is phase and amplitude self-calibrated on the continuum in the H_2CO spectral window using CASA 4.5 with timescales of 10–30 s. This improved the signal-to-noise ratio of the emission by a factor of ≈ 3 . Phase self-calibration is applied to the data from 2016.1.00311.S using line-free portions of the continuum. The solution interval is set to 30 s and polarization is averaged. Furthermore, the spectral windows are separately calibrated with a minimum signal-to-noise of 3 and minimum of 6 baselines per antenna. Data from 2016.1.00464.S is phase and amplitude self-calibrated with CASA 4.7.2 with two rounds of phase calibration, one over 30 s intervals and one over the integration time, and a single round of amplitude calibration. The signal-to-noise ratio in a CLEANed continuum image improved by a factor of ≈ 20 . The final calibration tables are applied to the line-containing spectral windows.

Subsequent data processing was performed with CASA 5.6.1 (McMullin et al. 2007). The continuum is subtracted using the UVCNTSUB task. Image reconstruction was performed with the TCLEAN algorithm using the multiscale deconvolver (Högbom 1974; Cornwell 2008) to reduce side lobes and increase the signal-to-noise ratio. Scales of $0''$, $0''.5$, $1''.0$, $2''.5$, and $5''.0$ were used for the multiscale deconvolver. No masking was applied as no significant difference was observed between the images with and without masking. Furthermore, masking creates a bias as scales used by the multiscale deconvolver larger than the masks are ignored by CLEAN. For the imaging of H_2CO $3_{03-2_{02}}$ Briggs weighting with a robust parameter of 0.5 was used, resulting in a synthesized beam of $0''.49 \times 0''.33$ and a good balance between the angular resolution and recovery of flux on all scales. All other H_2CO transitions were imaged with a robust parameter of 2.0, resulting in angular resolutions that closely match that of the $3_{03-2_{02}}$ line and optimizing the sensitivity. The $3_{12-2_{11}}$ transition is observed in only one

Table 1
ALMA Observations

ALMA Project Code	Date	Antennas	Baselines (m)	On-source (minutes)	Bandpass	Calibrators Phase	Flux
2013.1.00114.S ^a	2014 Jul 19 ¹	32	34-650	42.0	J1037-2934	J1037-2934	Pallas
2016.1.00311.S ^b	2016 Dec 16 ²	45	15-449	23.9	J1037-2934	J1037-2934	J1037-2934
	2017 Feb 1 ³	41	14-256	28.3	J1058+0133	J1037-2934	J1107-4449
	2017 Apr 8 ⁴	40	15-379	28.8	J1037-2934	J1037-2934	J1058+0133
	2017 May 5 ²	45	16-1120	39.3	J1037-2934	J1037-2934	J1107-4449
	2017 May 7 ²	51	16-1079	39.3	J1037-2934	J1037-2934	J1107-4449
	2017 May 21 ⁴	45	15-1097	47.8	J1037-2934	J1037-2934	J1037-2934
	2018 Jan 23 ³	43	14-1386	47.1	J1058+0133	J1037-2934	J1037-2934
2016.1.00464.S ^c	2018 Sep 20 ³	44	14-1385	47.1	J1037-2934	J1037-2934	J0904-5735
	2016 Dec 3 ⁵⁻⁷	40	14-662	48.3	J1058+0133	J1037-2934	J1037-2934
	2016 Dec 5 ⁵⁻⁷	46	15-648	48.3	J1058+0133	J1037-2934	J1058+0133
	2016 Dec 7 ⁵⁻⁷	45	14-609	48.3	J1058+0133	J1037-2934	J1037-2934
	2016 Dec 7 ⁵⁻⁷	45	15-648	48.3	J1058+0133	J1037-2934	J1058+0133
	2016 Dec 7 ⁵⁻⁷	39	15-596	48.3	J1058+0133	J1037-2934	J1037-2934
	2016 Dec 10 ⁵⁻⁷	46	15-648	48.3	J1058+0133	J1037-2934	J1058+0133
	2016 Dec 11 ⁵⁻⁷	46	15-636	48.3	J1058+0133	J1037-2934	J1037-2934

Notes. For (a), (b), and (c) the principal investigators are K. I. Öberg, L. I. Cleeves, and C. Walsh, respectively. (1)–(7) Link the transitions from Table 2 to the observation in which they are observed.

execution block with a Maximum Recoverable Scale (MRS) of $2''.3$, less than the size of the disk line emission in several channels. Therefore, for this specific transition some “smooth” flux on larger scales may be missing with the exact amount depending on the details of the imaging reconstruction (for example, simple CLEAN versus multiscale CLEAN as applied by us). Given that the emission is not “flat” and is primarily peaked toward the star, missing flux is not expected to be a large contributor to the overall flux.

All images were CLEANed to three times the noise found by the IMSTAT task in line-free channels. The spectral resolution (channel width) of all cubes was set to 0.25 km s^{-1} , close to the native resolution of the lowest resolution data (0.22 km s^{-1} for the $5_{15-4_{14}}$ transition). For several of the observed transition our data combine observations from different ALMA configurations and require corrections to obtain correct flux densities and noise levels. This stems from disparities between the flux scale in jansky per synthesized beam of the (CLEAN-recovered) emission and jansky per dirty beam for the noise residuals (R. A. Loomis et al. 2021, in preparation). A final flux calibration uncertainty of 10% is included in the further analysis as suggested by the ALMA Technical Handbook.

The CLEANed data cubes are masked according to the expected Keplerian rotation of TW Hya. Pixels are masked on a per channel basis where no emission is expected to occur when the emitting gas in the protoplanetary disk around TW Hya follows Keplerian rotation, (e.g., Salinas et al. 2017). The mask is created with the disk parameters: PA 152° , inclination 5° , and stellar mass $0.88 M_\odot$ from Huang et al. (2018) with a systematic velocity of 2.83 km s^{-1} (V_{LSR}) and outer radius of 220 au, which corresponds to the edge of the gas disk as measured by CO (Huang et al. 2018). Due to the nature of Keplerian masked moment-zero maps there is a nonuniform rms across the map, as described by Bergner et al. (2018), Pegues et al. (2020). We follow these authors and bootstrap the uncertainty of the moment-zero maps and integrated flux densities by evaluating the rms of a large number of extractions across a similar number of randomly chosen line-free channels.

3. Results

3.1. Observational Results

Emission in all seven targeted H_2CO transitions is clearly detected. Figure 1 shows the channel maps of the emission. Table 2 lists integrated flux densities of each transition extracted using Keplerian masking on the emission cubes. Values range from $1118 \pm 7 \text{ mJy km s}^{-1}$ for the o- H_2CO $5_{15-4_{14}}$ line to $22 \pm 4 \text{ mJy km s}^{-1}$ for the o- H_2CO $4_{32-3_{31}}$ line. Figure 2 shows the spectra integrated over the disk after Kepler masking.

The channel maps clearly show that the emission follows the velocity pattern of a disk in Keplerian rotation. Using the expected region of emission in each velocity channel integrated intensity (zero moment) maps are obtained and shown in Figure 3. These images show that the H_2CO emission is concentrated in a ring with a radius of $0''.3$ (18 au), with a broad fainter brim of emission as was also seen by Öberg et al. (2017). From these Keplerian masked integrated intensity images, radial emission profiles are extracted by annular averaging in 10 au wide bins (Figure 4). Uncertainty levels of the radially averaged intensities are calculated by dividing the moment-zero rms with the square-root of the number of independent beams present in that bin. To bring all data on the same angular resolution of $0''.5$, the H_2CO $3_{03-2_{02}}$, $4_{04-3_{03}}$, and $5_{15-4_{14}}$ were re-imaged using CLEAN and respective UVTAPER of $[0''.0, 0''.35, -87.8^\circ]$, $[0''.23, 0''.33, 64.7^\circ]$, and $[0''.18, 0''.30, 83.5^\circ]$ before the radial intensity profiles of these transitions were extracted. It should be noted that the $4_{31-3_{30}}$ and $4_{32-3_{31}}$ transitions have very similar excitation parameters and are thus difficult to distinguish in Figure 4.

3.2. H_2CO Excitation Temperature and Column Density

3.2.1. Rotational Diagram Analysis

The wide range of upper-state energies of 21–141 K of the detected H_2CO lines allow for well-constrained estimates of the excitation temperatures and column densities of the ortho and para isomers through a rotation diagram analysis (e.g., Goldsmith & Langer 1999). Since the gas densities in the disk (as estimated from the models of Cleeves et al. 2015; Kama et al. 2016)

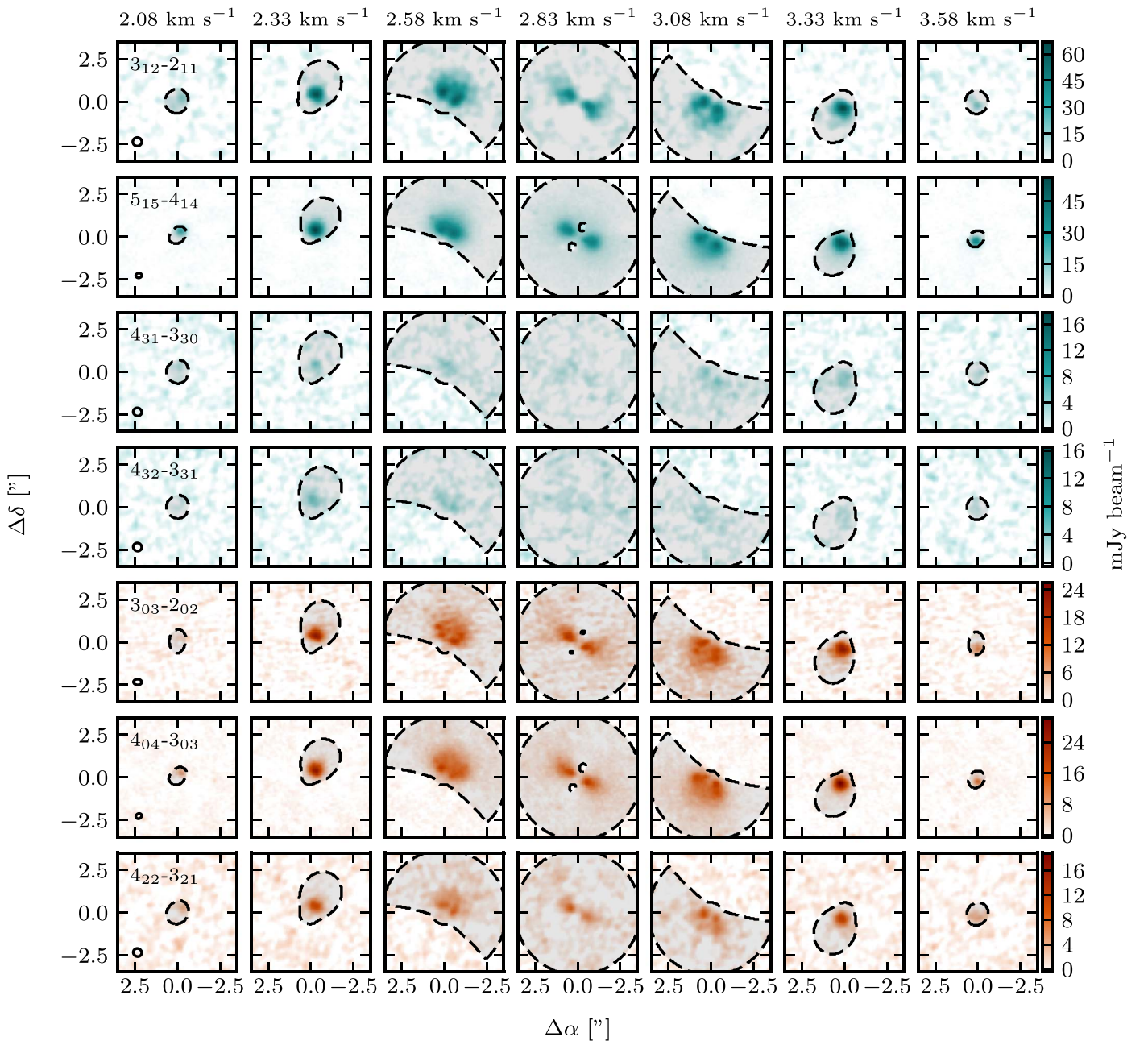


Figure 1. Channel maps from the observed transitions at native spatial resolution with the Keplerian masked overlaid. The channel velocities are labeled on top in the V_{LSR} reference frame. The teal and bronze color correspond to the ortho- and para-spin isomers, respectively. Beam sizes are indicated by the ellipse in the left-bottom corner of the first column.

typically exceed the critical density of the targeted transitions, $n_{\text{H}_2} \sim 10^6\text{--}10^7 \text{ cm}^{-3}$, the molecule's excitation is likely in local thermal equilibrium (LTE), even in the outer region of the disk. Derived excitation temperatures therefore are a reliable estimate of the kinetic temperature of the emitting gas, provided that the emission is optically thin. In the treatment outlined below, specific allowance is made for moderately optically thick emission.

The line intensity, I_ν , follows from the column density of the upper-state level in the optically thin limit, N_u^{thin} , as

$$I_\nu = \frac{A_{ul} N_u^{\text{thin}} hc}{4\pi \Delta\nu}, \quad (1)$$

where A_{ul} is the Einstein A coefficient and $\Delta\nu$ the velocity width of the emission line. Rewriting Equation (1) and

substituting the source brightness I_ν as flux per solid angle, S_ν/Ω , gives

$$N_u^{\text{thin}} = \frac{4\pi S_\nu \Delta\nu}{A_{ul} \Omega hc}. \quad (2)$$

Here, S_ν is the flux density extracted from the integrated spectra or the radial flux profiles, and Ω is the total solid angle from which the emission is extracted. If the emission is not fully optically thin, the column density of the upper-state level, N_u , follows from the optically thin limit by applying a correction for line optical depth,

$$N_u = N_u^{\text{thin}} \frac{\tau}{1 - e^{-\tau}}, \quad (3)$$

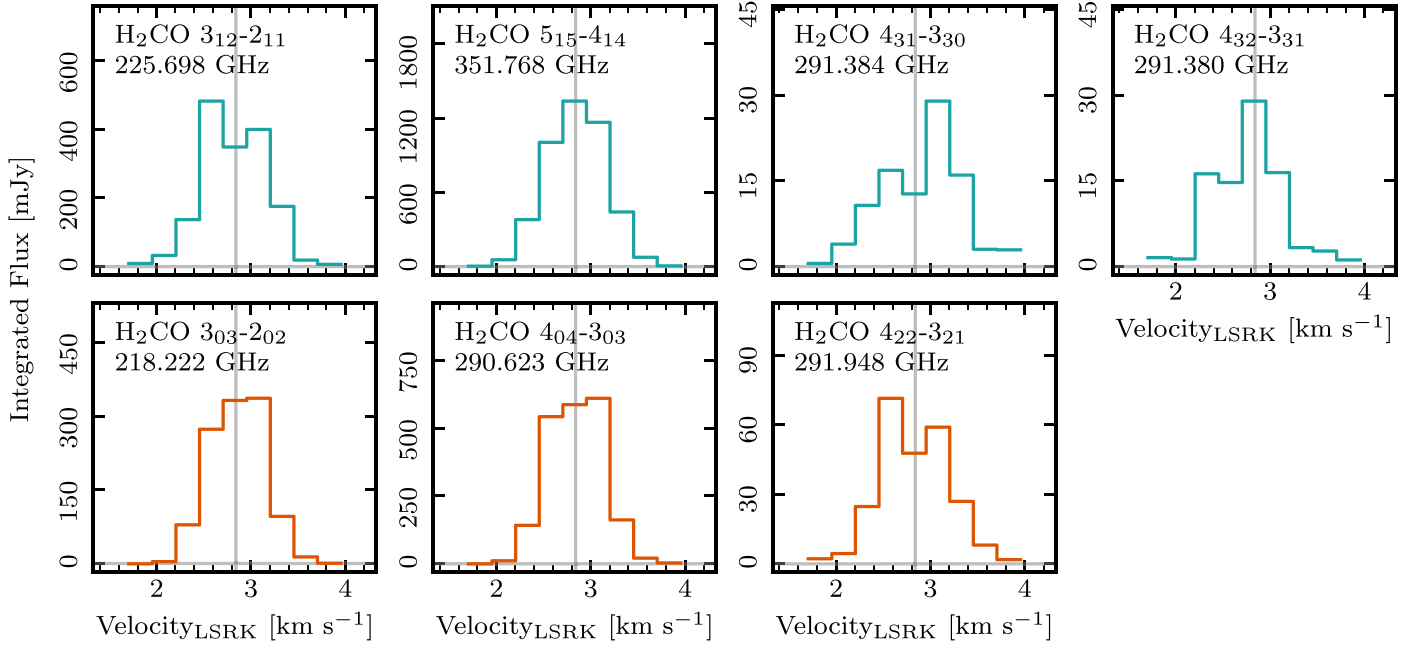


Figure 2. Integrated spectra of the seven observed Keplerian masked H₂CO transitions, i.e., pixels are masked according to a model predicting the Keplerian rotation of TW Hya. Top row, from left to right: o-H₂CO 3₁₂-2₁₁, 5₁₅-4₁₄, 4₃₁-3₃₀, and 4₃₂-3₃₁. Bottom row, from left to right: p-H₂CO 3₀₃-2₀₂, 4₀₄-3₀₃, and 4₂₂-3₂₁. The vertical line indicates the systematic velocity of TW Hya.

Table 2
Observed Formaldehyde Transitions

Transition	Log ₁₀ [A _{ij}] (s ⁻¹)	E _u (K)	Robust ^a	Beam ("×", °)	Channel rms ^b (mJy beam ⁻¹)	Mom-0 rms ^c (mJy beam ⁻¹ km s ⁻¹)	Int. Flux Density ^d (mJy km s ⁻¹)
3 ₀₃ -2 ₀₂ (p) ²	-3.55037	20.96	0.5	0.49 × 0.33, -87.8	1.46	0.49	283 ± 4
3 ₁₂ -2 ₁₁ (o) ¹	-3.55724	33.45	2.0	0.53 × 0.50, 88.7	2.65	0.98	402 ± 7
4 ₀₄ -3 ₀₃ (p) ³	-3.16102	34.90	2.0	0.35 × 0.29, 64.7	1.62	0.41	519 ± 5
4 ₂₂ -3 ₂₁ (p) ⁵	-3.27994	82.12	2.0	0.51 × 0.47, -60.3	0.93	0.36	62 ± 3
4 ₃₁ -3 ₃₀ (o) ⁶	-3.51653	140.9	2.0	0.51 × 0.47, -62.2	0.93	0.35	24 ± 4
4 ₃₂ -3 ₃₁ (o) ⁷	-3.51684	140.9	2.0	0.51 × 0.47, -62.2	0.93	0.36	22 ± 4
5 ₁₅ -4 ₁₄ (o) ⁴	-2.92013	62.45	2.0	0.35 × 0.28, 83.5	2.67	0.60	1118 ± 7

Notes. The rest frequency, Einstein A coefficient, and upper-state energy are taken from the LAMDA database. (1)–(7) Link the observations from Table 1 to the transitions.

^a The robust parameter used for Briggs weighting in the CLEAN process.

^b The channel rms is given at a common spectral resolution of 0.25 km s⁻¹.

^c The moment-zero rms is determined through the bootstrapping described in Section 2.

^d The integrated flux density is retrieved through summation of the emission retrieved by Keplerian masking of the emission cube.

where τ is the optical depth at the center of the line. This line opacity τ is given by

$$\tau = \frac{A_{ul}N_u^{\text{thin}}c^3}{8\pi\nu^3\Delta\nu}(e^{h\nu/kT_{\text{rot}}} - 1), \quad (4)$$

where ν is the rest frequency of the transition. An upper limit to the opacity follows from assuming a line width $\Delta\nu$ equal to the disk-averaged FWHM of the intrinsic line, estimated to be 0.275 km s⁻¹. This value is estimated from the FWHM of the Keplerian corrected integrated spectra acquired with GOFISH (Teague 2019). Finally, the total column density, N_{tot} , is related to the upper-state level populations through the Boltzmann equation,

$$\frac{N_u}{g_u} = \frac{N_{\text{tot}}}{Q(T_{\text{rot}})}e^{-E_u/kT_{\text{rot}}}, \quad (5)$$

where g_u is the degeneracy of the corresponding upper-state level, Q the partition function of H₂CO, E_u the upper-state level energy, and T_{rot} the rotational temperature of H₂CO. The upper-state degeneracy, upper-state energy, Einstein A coefficient, and frequency of each transition are extracted from the Leiden Atomic and Molecular Database (LAMDA; Schöier et al. 2005). The partition function for H₂CO is constructed from the rotational ground states taken from the ExoMol database (Al-Refaie et al. 2015; Wang et al. 2020). In order to independently investigate the nuclear-spin isomers a separate partition function is created for each of the isomers. The ExoMol database assumes an OPR of three. This OPR is incorporated in their state degeneracies and is removed by dividing by three to match the state degeneracies of the LAMDA database. The partition function is constructed

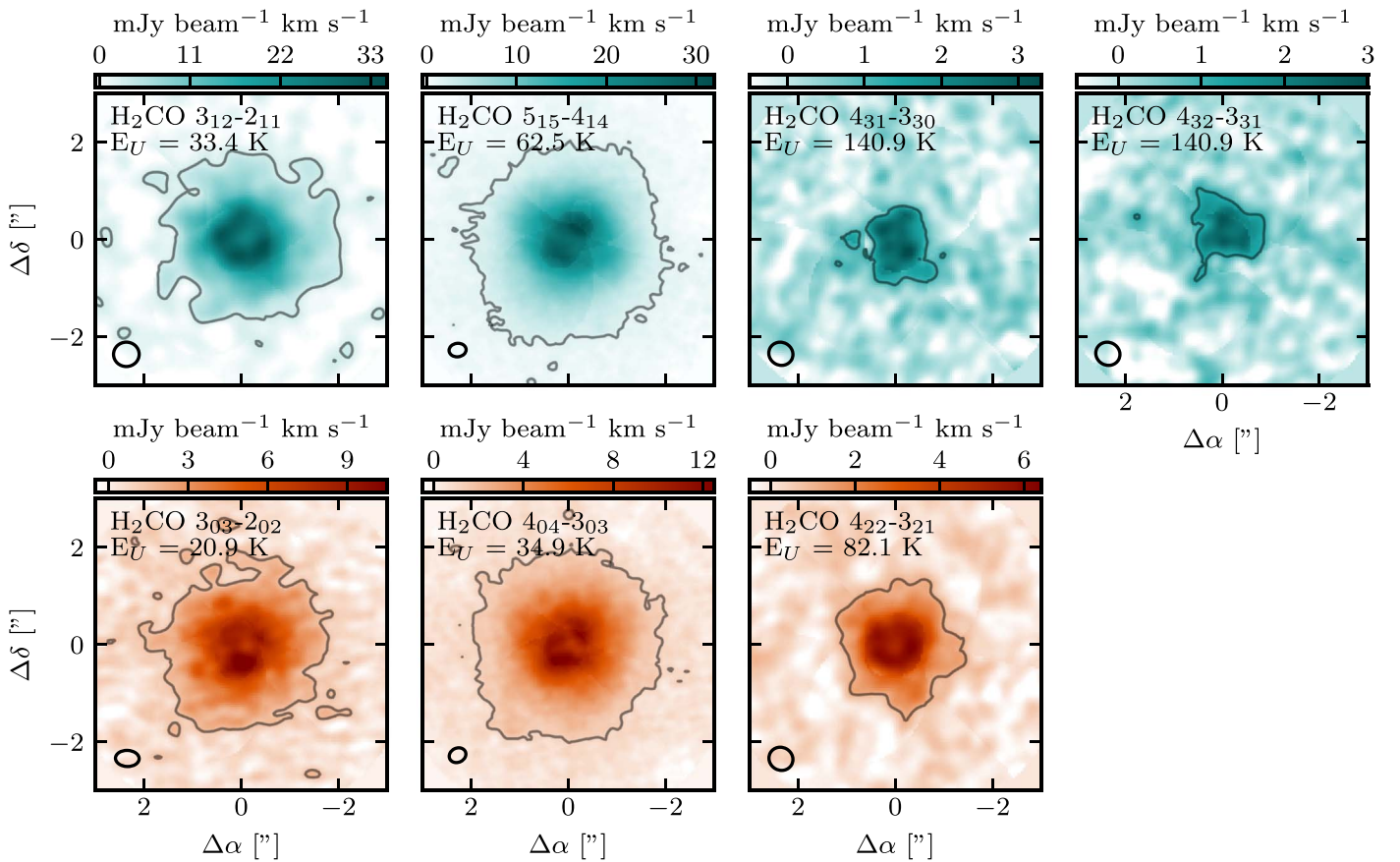


Figure 3. Keplerian masked velocity integrated emission of observed H₂CO transitions at native spatial resolution ($V_{\text{LSR}} = 1.83\text{--}3.83 \text{ km s}^{-1}$). Top row: ortho-spin isomer transitions; bottom row: para-spin isomer transitions. The contour in each panel depicts 3σ , where σ for each transition is taken from Table 2. Beam sizes are indicated by the ellipse in the left-bottom corner of each panel.

by summing over the possible internal H₂CO ground states,

$$Q(T_{\text{rot}}) = \sum_i g_i e^{-E_i/kT}, \quad (6)$$

where g_i is the degeneracy and E_i the energy of state i . These separate partition functions allow independent determination of the column densities of each spin isomer. As is customary for rotation diagram analyses, the column density N_{tot} and rotation temperature T_{rot} are retrieved from the intercept and slope, respectively, of $\ln(N_u/g_u)$ versus E_u (Figure 5). Following Loomis et al. (2018) and Teague et al. (2018), we create a likelihood function from Equation (5) and use EMCEE (Foreman-Mackey et al. 2013) to retrieve posterior distributions for T_{rot} and N_{tot} from the observed H₂CO transitions. This rotational diagram fitting procedure is applied to each of the spin isomers separately.

3.2.2. Disk-averaged Rotational Diagram

The disk-integrated flux densities of Table 2, analyzing each spin isomer separately, yields disk-averaged column densities and rotational temperatures of $(1.1 \pm 0.1) \times 10^{12} \text{ cm}^{-2}$, $33 \pm 2 \text{ K}$ and $(4.3 \pm 0.3) \times 10^{11} \text{ cm}^{-2}$, $25 \pm 2 \text{ K}$ for ortho- and para-H₂CO, respectively. These values result in a disk-averaged OPR of 2.49 ± 0.23 . Uncertainties are the 16th and 84th percentiles of the posterior distributions, corresponding to 1σ . The disk-averaged line opacities range from 0.002–0.049, confirming the assumption of optically thin emission. However,

one should note that this assumes a uniform distribution of H₂CO across the entire disk which is not the case, as seen in Figure 4. The opacities will be larger in the inner region where column densities are higher, as shown in Section 3.2.3.

Carney et al. (2019) investigated the disk-averaged ratio of CH₃OH with respect to H₂CO for the protoplanetary disks around HD 163296 and TW Hya. Specifically for TW Hya they found a CH₃OH/H₂CO ratio of 1.27 ± 0.13 . In their work the average H₂CO and CH₃OH column densities are derived self-consistently from the integrated line intensity of one transition and an assumed excitation temperature, (see Equation (1) Carney et al. 2019). The H₂CO column density is found to be $3.7 \times 10^{12} \text{ cm}^{-2}$, which is approximately 2.4 times higher than the derived average total H₂CO column density of $(1.5 \pm 0.1) \times 10^{12} \text{ cm}^{-2}$ in this work. The lower total H₂CO column density derived through rotational diagram analysis pushes the CH₃OH/H₂CO ratio up to a value of 3.1 ± 0.4 . However, it should be noted that the CH₃OH column density used in this work is taken from Carney et al. (2019) and is thus not derived self-consistent with the H₂CO column density.

The rotational temperatures of both spin isomers are not identical, with a slightly higher value of 33 K found for ortho-H₂CO compared to 26 K for para-H₂CO. If the OPR is in thermal equilibrium, such a difference is expected: the ortho isomer is the more abundant in warmer gas compared to the para isomer, resulting in a higher rotational temperature for the former when averaging its emission over the disk. However, there may also be a systematic bias, because the detected o-H₂CO lines extend over a larger range of upper-level energies (up to 141 K)

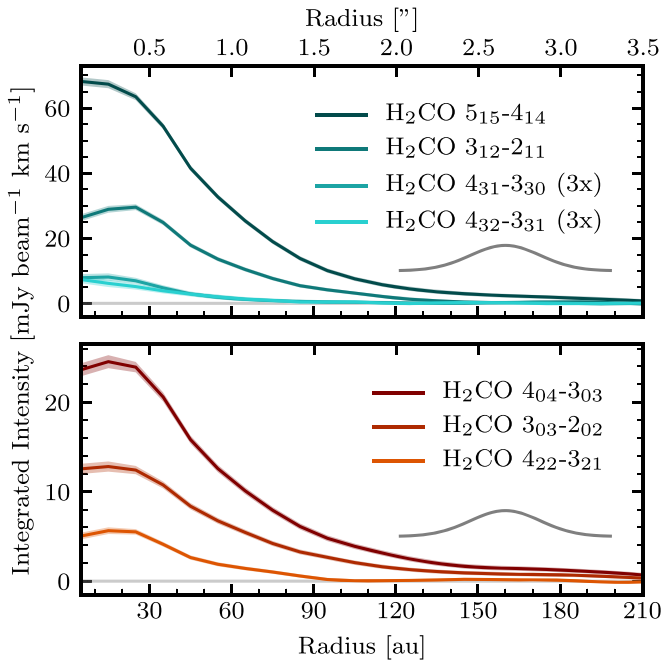


Figure 4. Radial intensity profiles of the observed ortho (top panel) and para (bottom panel) H₂CO transitions retrieved from the Keplerian masked moment-zero maps. The displayed uncertainties do not contain the 10% flux calibration error. All data have a common spatial resolution of 30 au depicted by the Gaussian in the bottom right.

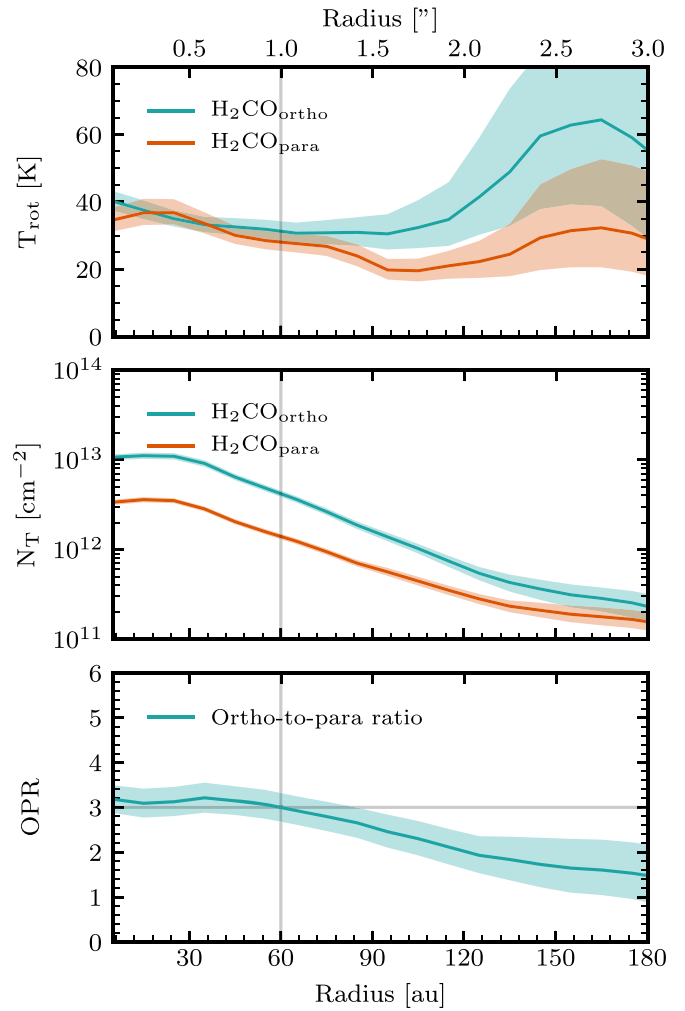


Figure 6. Radially resolved H₂CO temperature (top panel), column densities (middle panel), and OPR (bottom panel) of H₂CO obtained from our rotational diagram analysis using the radial emission profiles of Figure 4. The teal and bronze colors represent the ortho- and para-spin isomers, respectively. The shaded areas depict 1σ uncertainties. The gray vertical and horizontal lines depict the millimeter-dust continuum edge and the high temperature OPR limit of 3.0, respectively.

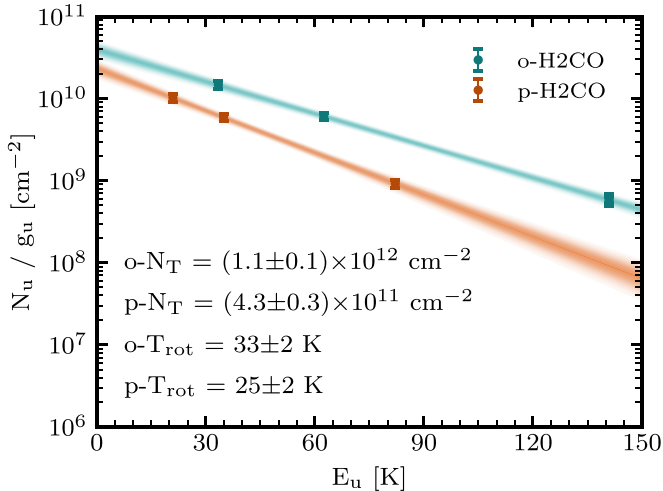


Figure 5. Rotational diagram of disk-averaged H₂CO flux density values from Table 2. The teal and bronze color represent the level populations of the ortho- and para-spin isomers, respectively. The markers show the data and the lines show random draws from the posterior distribution retrieved by the EMCEE fitting procedure.

compared to the p-H₂CO lines (up to 82 K), thus naturally probing higher excitation gas. Section 3.2.3 explores further explanations, folding in spatially resolved information.

3.2.3. Radially Resolved Rotational Diagram

The same rotational diagram analysis as carried out above for the disk-integrated fluxes, can also be performed as function of radius, using the Keplerian masked moment-zero images, all restored to a common resolution of $0''.5$, and the corresponding radial intensity profiles of Figure 4. As depicted in Figure 6, the

column densities in the $0''.5$ beam peak at ~ 20 au with values of $(1.1 \pm 0.1) \times 10^{13} \text{ cm}^{-2}$ and $(3.6 \pm 0.3) \times 10^{12} \text{ cm}^{-2}$ for o-H₂CO and p-H₂CO, respectively. The opacities are largest in the inner region where column densities are highest. The largest optical depths are found to be $\tau = 0.47$ and $\tau = 0.35$ for the $5_{15-4_{14}}$ and $3_{12-2_{11}}$ transition, respectively. Beyond 85 au all the opacities drop to a value of $\tau < 0.1$. Therefore, all transitions only require a moderate correction for opacity.

The rotational temperatures of both the ortho- and para-H₂CO are found to be consistent with each other within 80 au. The averaged rotational temperatures drops as function of radius from 37 ± 5 K at the center of the first radial bin (5 au), to 29 ± 5 K at 75 au. These observed rotational temperature are below the freeze-out temperature of gas-phase H₂CO at approximately 80 K (Noble et al. 2012; Pegues et al. 2020). Beyond 80 au the rotational temperatures deviate from each other with a two sigma tension. This explains the observed difference in rotational temperatures from the disk-averaged analysis. At radii beyond 120 au no meaningful constraints on the temperature are found due to the low signal-to-noise ratio in the majority of the transitions.

The observed temperature difference between the ortho- and para-spin isomer from the disk-averaged analysis can be traced back to two transitions: $3_{12}-2_{11}$ and $4_{22}-3_{21}$. The $3_{12}-2_{11}$ transition is observed with an MRS of $2''3$. This transition has an upper-state energy of 33 K, the lowest of the ortho-spin isomers in this data set. With potentially missing extended emission on scales of $2''3$ and larger, the fit may result in higher rotational temperatures on these scales. The $4_{22}-3_{21}$ transition has an upper-state energy of 82 K, which is the highest of the para-spin isomers in this data set. Combined with the drop in emission of the radial profile from 90–140 au, this may result in lower rotational temperatures in this region. Additional observations with a more robust coverage of the extended emission are needed to determine the H_2CO emitting temperature more robustly.

Dividing the column density profiles of o- H_2CO and p- H_2CO yields the radially resolved OPR, which is consistent with an OPR of 3.0, the high temperature limit, in the inner 60 au and drops to lower values at larger radii, e.g., 2.0 ± 0.5 at a distance of 120 au. We rule out that the temperature bias described in the previous paragraph has an impact on the derived OPR. Repeating the analysis at fixed rotational temperatures ranging from 30–40 K, and omitting the $3_{12}-2_{11}$ transition that may miss extended emission, we recover the same downward OPR trend. The fixed rotational temperature model of 35 K is shown in Figure 7. We therefore conclude that the radial decrease in the OPR beyond the millimeter-dust continuum is robust.

4. Discussion

4.1. The Inner H_2CO Line Emission Decrease

Our resolved, multiline observations of H_2CO in TW Hya broadly indicate a flattening or decrease in flux interior to 20 au. An inner deficit in the intensity profile has been seen in other disks and other molecular lines, and can be attributed either to real decreases in column density or to line or continuum opacity (Andrews et al. 2012; Cleeves et al. 2016; Isella et al. 2016; Loomis et al. 2017). Continuum over-subtraction due to optically thick lines can be ruled out in this case, given the consistently low optical line depths (<0.5 , see Section 3.2). Continuum opacity is also likely not the only explanation, because emission of other molecules at similar wavelengths are centrally peaked (e.g., $\text{C}^{18}\text{O } J=3-2$ imaged by Schwarz et al. 2016). However, it should be noted that Huang et al. (2018) found the millimeter wavelength spectral index inside <20 au to be 2.0, indicative of optically thick continuum emission. Depending on the height where the line emission originates, some of the drop in emission may be due to an optically thick continuum. Nonetheless, our data show evidence of H_2CO inside of 20 au, the approximate CO snow line location in this disk (Schwarz et al. 2016; van’t Hoff et al. 2017; Zhang et al. 2017), indicative of active gas-phase H_2CO chemistry as was also found in Öberg et al. (2017).

4.2. Gas-phase versus Grain-surface Formation of H_2CO

In interstellar environments, H_2CO forms by a combination of CO-ice hydrogenation and neutral-neutral gas-phase reactions, specifically $\text{CH}_3 + \text{O}$ and $\text{CH}_2 + \text{OH}$ (e.g., Loomis et al. 2015). For CO ice to exist in abundance, the dust grain temperature must be quite low, below 25 K depending on the binding surface. This temperature is much lower than the

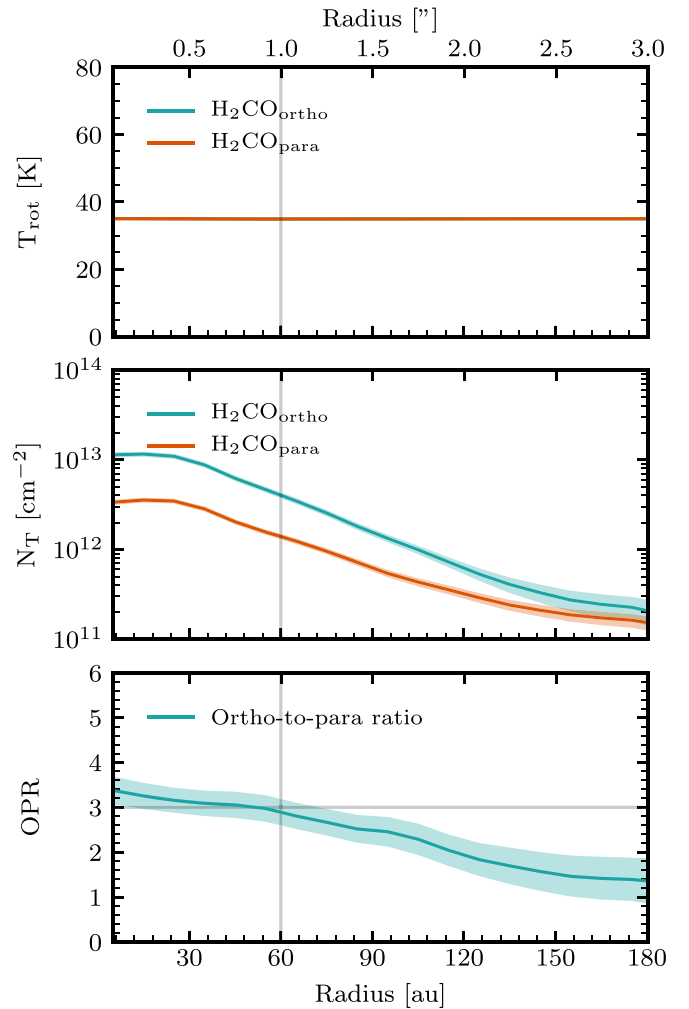


Figure 7. Radially resolved H_2CO temperature (top panel), column densities (middle panel), and OPR (bottom panel) of H_2CO obtained from our rotational diagram analysis with a fixed rotational temperature at 35 K. The teal and bronze colors represent the ortho- and para-spin isomers, respectively. The shaded areas depict 1σ uncertainties. The gray vertical and horizontal lines depict the millimeter-dust continuum edge and the high temperature OPR limit of 3.0, respectively.

thermal desorption temperature of H_2CO , therefore H_2CO formed by this mechanism requires subsequent nonthermal desorption to produce observable gas-phase quantities. Previous work by Loomis et al. (2015) and Öberg et al. (2017) found that a combination of gas-phase and solid-state chemistry likely contributes to the observed gaseous H_2CO in disks. In TW Hya specifically, Öberg et al. (2017) suggested that the H_2CO ring near the CO snow line could be evidence of a CO-ice regulated chemistry (see also Qi et al. 2013). In addition, a number of sources, e.g., HD 163296, CI Tau, DM Tau, and AS 209 (see Pegues et al. 2020), show an increase or ring in H_2CO in the outer disk. A clear example of a secondary increase is found in HD 163296 at a radius of ~ 250 au (Carney et al. 2017). These authors suggest that an additional formation route related to CO ice may be opening up at this location, or that increased penetration of ultraviolet radiation boosts gas-phase formation of H_2CO .

Previous work by Öberg et al. (2017) showed a similar emission bump in the $3_{12}-2_{11}$ transition near the millimeter-dust continuum edge at 60 au. Our imaging of the same data at similar spatial resolution does not show this emission bump.

We attribute the difference to the MRS of 2/3 of this data set in combination with the different applied CLEAN method (multiscale CLEAN), since this method is expected to yield a more reliable result for extended emission.

The near-constant rotational temperature of 30–40 K found here for H₂CO suggests that the emission arises from an elevated layer in TW Hya’s disk, well above the CO snow surface. In models of the TW Hya disk (Bergin et al. 2013; Cleeves et al. 2015; Kama et al. 2016; Calahan et al. 2020), these temperatures are found at normalized heights of $z/R \geq 0.25$. Additionally, recent observations of the edge-on younger embedded disk IRAS 04302 also show that the bulk of the H₂CO emission arises from $z/R \sim 0.21$ – 0.28 (Podio et al. 2020; van’t Hoff et al. 2020). At these heights, sufficient UV can penetrate to induce photodesorption of H₂CO since the bulk of the small dust has grown and is very settled (e.g., Dullemond & Dominik 2004; Testi et al. 2014). These same UV photons also induce efficient gas-phase formation of H₂CO by radical production, since the two radical-radical gas-phase reactions that form H₂CO are barrierless. Teague & Loomis (2020) found CN at similar heights in TW Hya, a molecule which is formed mainly through UV irradiation (Cazzoletti et al. 2018). Our data therefore suggest that gas-phase formation is likely important to explain the observed gas-phase H₂CO across the entire disk of TW Hya.

Interestingly, Loomis et al. (2015) found that gas-phase chemistry alone underproduced the observed column density of H₂CO in the DM Tau protoplanetary disk. However, it is important to note that the modeling carried out in Loomis et al. (2015) either fully turned off CO hydrogenation or left on the full CO-hydrogenation pathway up to forming CH₃OH. While detailed chemical modeling is beyond the scope of the present paper, we examined the reaction rates from the existing Cleeves et al. (2015) TW Hya chemical model with a dust surface area reduction of 85%. The latter is invoked to emulate the effects of dust settling and radial drift, which significantly reduce the effective solid surface for ice chemistry to occur (Hogerheijde et al. 2011; Bergin & Cleeves 2018). In the layer where H₂CO is abundant ($z/R > 0.25$), the two gas-phase pathways with O and OH are far more efficient than CO-ice hydrogenation due to the warm temperatures of the surface layers. From these initial tests it also appears that, although H₂CO formed in the gas phase is easily photodissociated, subsequent freeze-out of the resulting HCO radicals reforms H₂CO, as the hydrogenation step involved is barrierless (Fuchs et al. 2009). Further modeling is needed to confirm this symbiotic gas-grain relationship in H₂CO formation. The key role of UV-induced gas-phase chemistry has been seen in other models. Walsh et al. (2014) find that H₂CO can be efficiently formed through gas-phase chemistry alone around a typical T Tauri star. They found a fractional abundance with respect to n_{H} of 10^{-10} – 10^{-9} , which translates in their models to column densities between 10^{12} and 10^{13} cm⁻², very similar to the values obtained from our observations. It should be noted that although gas-phase chemistry is sufficient to explain observed *gas-phase* column densities it does not imply that *solid-state* formation does not occur in the disk midplane. The chemical models generally produce five orders of magnitude more solid-state H₂CO in the disk midplane.

4.3. Constraints from the H₂CO OPR on the Formation

The smooth radial H₂CO column density profile and near-constant excitation temperature are consistent with a single origin of the observed H₂CO, namely gas-phase formation. Is this

consistent with the radial gradient in OPR that is also observed? As first proposed by Kahane et al. (1984), the OPR of H₂CO—if distributed according to a Boltzmann distribution—drops below 3.0 for spin temperatures below ~ 35 K and reaches 2.0 for a spin temperature of ~ 12 K (see Figure 10 of Kahane et al. 1984). The spin temperature is thought to correspond to the formation temperature of the molecule since the gas-phase nuclear-spin conversion time for nonreactive collisions is longer than the H₂CO lifetime (Tudorie et al. 2006). Within 60 au, the inferred *rotational* temperatures of 30–40 K are consistent with the *spin* temperatures of $\gtrsim 27$ K found from the OPR. Outside 60 au, and especially outside 120 au, the OPR suggest a spin temperature of 10–17 K, while the (poorly constrained) rotational temperature exceeds 20 K (1σ).

A low OPR and corresponding low formation temperature have been invoked as evidence of the formation of H₂CO in the ice, during the prestellar phase or in cold regions of the disk, and subsequent release in the gas. This is based on the expectation that the OPR is conserved from the moment of formation, because radiative transitions between ortho- and para-H₂CO are strictly forbidden. However, recent experimental work by Hama et al. (2018) showed that nonthermal desorption of para-enriched water ice at 11 K causes the OPR to revert to 3.0, as expected for higher temperatures. For water, this is explained by the fact that water molecules in the ice cannot rotate because of hydrogen bonds in the ice matrix. This restriction results in a quasi-degeneracy of the ortho- and para-H₂O states in the solid state. Furthermore, theoretical studies on solid-state H₂O propose that rapid nuclear-spin conversion in the solid-state is possible through intermolecular proton–proton magnetic dipolar interactions (Limbach et al. 2006; Buntkowsky et al. 2008). Similar to H₂O, H₂CO will also be rotationally hindered in the solid state, and an OPR of 3.0 may be expected on release into the gas phase, even when formed at low temperatures. However, the extent of rotational hindrance of H₂CO in an apolar CO matrix has to be investigated theoretically or experimentally before a conclusive statement can be made.

If we accept that the OPR reflects the temperature of the H₂CO formation in the ice, our observed values indicate that only outside 60 au does the observed H₂CO emission contain a contribution originating in the ice. Although not very well constrained, the rotational temperature at these radii exceeds the freeze-out temperature of CO, < 21 K (Schwarz et al. 2016), suggesting that some vertical transport of H₂CO formed in the midplane through hydrogenation is required. Given the low turbulence in the TW Hya disk (Flaherty et al. 2018), it is not immediately clear what mechanism can efficiently explain this vertical transport. Alternatively, solid-state H₂CO can be inherited from the prestellar stage (e.g., Visser et al. 2011). This inherited H₂CO ice could then non-thermally desorb in an elevated layer in the protoplanetary disk stage before it settles to the disk midplane. If, however, the observed H₂CO has an inherited origin and we assume the OPR is preserved we would expect a constant value. The observed OPR ranging from 3.0–2.0 in this single monotonic component would thus require an external influence, e.g., different desorption conditions or subsequent disk gas-phase chemistry. This inherently implies that the OPR of the inherited ice is not wholly preserved. It is possible that due to beam smearing multiple components are hidden in what now seems to be a single component. However,

the OPR drops across three beam sizes making this scenario unlikely.

If, on the other hand, we accept that the OPR is reset to 3.0 on desorption as suggested by the experiments discussed above, the lower OPR values found outside 60 au mean that ice formation cannot play a significant role here. Instead, gas formation is required. To explain the low OPR requires either low-temperature formation or a *chemical* explanation. The former can be explained by deeper penetration of UV radiation at large radii, producing the required radicals closer to the midplane and at lower temperatures. The latter requires detailed modeling including the spin state chemistry and the role of H₂ spin. The extent to which the *rotational* temperature in the outer disk deviates from the *spin* temperature corresponding to the observed OPR cannot be assessed with the current data. Future ALMA observations with higher signal-to-noise and additional transitions with lower upper-state energies are needed for this.

Additionally, in this scenario the observed OPR of 3.0 inside 60 au is both consistent with gas-phase formation and nonthermal desorption from the solid state. However, H₂CO formed in the solid state from CO hydrogenation during the protoplanetary disk stage requires vertical transport, which is unlikely in TW Hya due to the lack of turbulence, as described above. This raises the question, what does create the H₂CO ring emission at ~ 20 au if it is not linked to the CO snowline? The observations of the edge-on younger embedded disk IRAS 04302 also found that H₂CO decreases in the inner region (Podio et al. 2020; van't Hoff et al. 2020). In this younger and warmer disk, CO does not freeze-out due to higher midplane temperatures (van't Hoff et al. 2018). Furthermore, C¹⁷O emission in the IRAS 04302 disk does not decrease in the inner region, ruling out dust opacity (van't Hoff et al. 2020). The authors thus argue that the decrease of H₂CO in the inner region is due to lower abundances of parent radicals in the gas-phase instead of an optically thick continuum. This mechanism could still be at play in an older protoplanetary disk like TW Hya and will be investigated in a follow-up paper with chemical modeling.

5. Summary

We report the most comprehensive survey of spatially and spectrally resolved ortho- and para-H₂CO emission in a protoplanetary disk to date, TW Hya. We detect H₂CO emission across the entire disk out to 180 au, with a partially filled emission ring at 20 au and a smooth decrease beyond this radius. A rotational diagram analysis shows that the emission originates from a layer with a nearly constant temperature between 30 and 40 K, which corresponds to $z/R \geq 0.25$. We find column densities of a few times 10^{13} cm⁻² in the inner disk decreasing to $\sim 10^{12}$ cm⁻² in the outer disk, and an OPR consistent with 3 in the inner 60 au decreasing to a value of ~ 2 at 120 au. Unlike some other disks, e.g., HD 163296, CI Tau, DM Tau, and AS 209, no secondary increase in the H₂CO emission or column density is seen in the outer disk. The results and discussion presented in this work have led us to speculate that the low OPR of H₂CO in the disk of TW Hya does not reflect direct ice formation, as is commonly assumed, but instead hints at predominantly gas-phase formation. Several lines of evidence lead to this speculation: (1) the smooth emission profiles that suggests a single formation path across the disk, (2) the radially decreasing OPR, (3) the lack of vertical mixing to return H₂CO ice from the disk midplane, and

(4) the recent results on the reset of the OPR to 3 upon desorption of H₂O. Instead, a cold *gas-phase* origin of the gaseous H₂CO molecules responsible for the emission appears a more likely scenario for TW Hya. In other disks (e.g., DM Tau, Loomis et al. 2015), ice formation may play a larger role, and even in TW Hya the *bulk* of the H₂CO likely resides (unobserved) in ice near the midplane. Gas-phase formation is supported by the presence of abundant H₂CO in the same region where there is a deficit of solid mass, specifically outside of the millimeter pebble disk. This is the same region where the OPR begins to drop. This scenario will be tested in a follow-up study with forward models that include chemistry, spin states, and radiative transfer to better understand the observed OPR and its implications for organic formation in disks during planet formation.

The authors thank the anonymous referee for the constructive feedback on this manuscript. The authors acknowledge the help with the ALMA data processing by Allegro, the European ALMA Regional Center node in the Netherlands; Allegro is funded by NWO, the Netherlands Organisation for Scientific Research. This paper makes use of the following ALMA data:

1. ADS/JAO.ALMA#2013.1.00114.S,
2. ADS/JAO.ALMA#2016.1.00311.S,
3. ADS/JAO.ALMA#2016.1.00464.S.







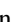



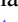




ALMA is a partnership of ESO (representing its member states), NSF (USA) and NINS (Japan), together with NRC (Canada), MOST and ASIAA (Taiwan), and KASI (Republic of Korea), in cooperation with the Republic of Chile. The Joint ALMA Observatory is operated by ESO, AUI/NRAO and NAOJ. The National Radio Astronomy Observatory is a facility of the National Science Foundation operated under cooperative agreement by Associated Universities, Inc. J.T.v.S. and M.R.H. are supported by the Dutch Astrochemistry II program of the Netherlands Organization for Scientific Research (648.000.025). L.I.C. gratefully acknowledges support from the David and Lucille Packard Foundation, the VSGC New Investigators Award, and NASA ATP 80NSSC20K0529. C.W. acknowledges financial support from the University of Leeds and from the Science and Technology Facilities Council (Grant Nos. ST/R000549/1 and ST/T000287/1). J.K.C. acknowledges support from the National Science Foundation Graduate Research Fellowship under Grant No. DGE 1256260 and the National Aeronautics and Space Administration FINESST grant, under Grant No. 80NSSC19K1534. V.V.G. acknowledges support from FONDECYT Iniciación 11180904. J.H. acknowledges support for this work provided by NASA through the NASA Hubble Fellowship Grant No. HST-HF2-51460.001-A awarded by the Space Telescope Science Institute, which is operated by the Association of Universities for Research in Astronomy, Inc., for NASA, under contract NAS5-26555. “M.K. gratefully acknowledges funding by the University of Tartu ASTRA project 2014–2020.4.01.16-0029 KOMEET, financed by the EU European Regional Development Fund.

ORCID iDs

Jeroen Terwisscha van Scheltinga  <https://orcid.org/0000-0002-3800-9639>

Michiel R. Hogerheijde  <https://orcid.org/0000-0001-5217-537X>

L. Ilseidore Cleaves  <https://orcid.org/0000-0003-2076-8001>

Ryan A. Loomis  <https://orcid.org/0000-0002-8932-1219>
 Catherine Walsh  <https://orcid.org/0000-0001-6078-786X>
 Karin I. Öberg  <https://orcid.org/0000-0001-8798-1347>
 Edwin A. Bergin  <https://orcid.org/0000-0003-4179-6394>
 Jennifer B. Bergner  <https://orcid.org/0000-0002-8716-0482>
 Geoffrey A. Blake  <https://orcid.org/0000-0003-0787-1610>
 Jenny K. Calahan  <https://orcid.org/0000-0002-0150-0125>
 Paolo Cazzoletti  <https://orcid.org/0000-0002-1917-7370>
 Ewine F. van Dishoeck  <https://orcid.org/0000-0001-7591-1907>
 Viviana V. Guzmán  <https://orcid.org/0000-0003-4784-3040>
 Jane Huang  <https://orcid.org/0000-0001-6947-6072>
 Mihkel Kama  <https://orcid.org/0000-0003-0065-7267>
 Chunhua Qi  <https://orcid.org/0000-0001-8642-1786>
 Richard Teague  <https://orcid.org/0000-0003-1534-5186>
 David J. Wilner  <https://orcid.org/0000-0003-1526-7587>

References

- Aikawa, Y., Momose, M., Thi, W.-F., et al. 2003, *PASJ*, **55**, 11
 Aikawa, Y., van Zadelhoff, G. J., van Dishoeck, E. F., & Herbst, E. 2002, *A&A*, **386**, 622
 Akiyama, E., Muto, T., Kusakabe, N., et al. 2015, *ApJL*, **802**, L17
 Al-Refaie, A. F., Yachmenev, A., Tennyson, J., & Yurchenko, S. N. 2015, *MNRAS*, **448**, 1704
 Andrews, S. M., Wilner, D. J., Hughes, A. M., et al. 2012, *ApJ*, **744**, 162
 Andrews, S. M., Wilner, D. J., Zhu, Z., et al. 2016, *ApJL*, **820**, L40
 Atkinson, R., Baulch, D. L., Cox, R. A., et al. 2006, *ACP*, **6**, 3625
 Bergin, E. A., & Cleeves, L. I. 2018, *Chemistry During the Gas-Rich Stage of Planet Formation*, in *Handbook of Exoplanets*, ed. H. Deeg & J. Belmonte (Cham: Springer), 137
 Bergin, E. A., Cleeves, L. I., Gorti, U., et al. 2013, *Natur*, **493**, 644
 Bergner, J. B., Guzmán, V. G., Öberg, K. I., Loomis, R. A., & Pegues, J. 2018, *ApJ*, **857**, 69
 Buntkowski, G., Limbach, H.-H., Walaszek, B., et al. 2008, *Z. Phys. Chem.*, **222**, 1049
 Calahan, J., Bergin, E., Zhang, K., et al. 2020, *ApJ*, accepted (arXiv:2012.05927)
 Carney, M. T., Hogerheijde, M. R., Guzmán, V. V., et al. 2019, *A&A*, **623**, A124
 Carney, M. T., Hogerheijde, M. R., Loomis, R. A., et al. 2017, *A&A*, **605**, A21
 Cazzoletti, P., van Dishoeck, E. F., Visser, R., Facchini, S., & Bruderer, S. 2018, *A&A*, **609**, A93
 Chuang, K. J., Fedoseev, G., Qasim, D., et al. 2017, *MNRAS*, **467**, 2552
 Cleeves, L. I., Bergin, E. A., Qi, C., Adams, F. C., & Öberg, K. I. 2015, *ApJ*, **799**, 204
 Cleeves, L. I., Öberg, K. I., Wilner, D. J., et al. 2016, *ApJ*, **832**, 110
 Cornwell, T. J. 2008, *ISTSP*, **2**, 793
 Dullemond, C. P., & Dominik, C. 2004, *A&A*, **421**, 1075
 Dutrey, A., Guilloteau, S., & Guélin, M. 1997, *A&A*, **317**, L55
 Fedoseev, G., Chuang, K. J., Ioppolo, S., et al. 2017, *ApJ*, **842**, 52
 Flaherty, K. M., Hughes, A. M., Teague, R., et al. 2018, *ApJ*, **856**, 117
 Fockenberg, C., & Preses, J. M. 2002, *JPCA*, **106**, 2924
 Foreman-Mackey, D., Hogg, D. W., Lang, D., & Goodman, J. 2013, *PASP*, **125**, 306
 Fuchs, G. W., Cuppen, H. M., Ioppolo, S., et al. 2009, *A&A*, **505**, 629
 Gaia Collaboration, Brown, A. G. A., Vallenari, A., et al. 2018, *A&A*, **616**, A1
 Garufi, A., Podio, L., Codella, C., et al. 2020, *A&A*, **636**, A65
 Goldsmith, P. F., & Langer, W. D. 1999, *ApJ*, **517**, 209
 Guzmán, V. V., Öberg, K. I., Carpenter, J., et al. 2018, *ApJ*, **864**, 170
 Hama, T., Kouchi, A., & Watanabe, N. 2018, *ApJL*, **857**, L13
 Herbst, E., & van Dishoeck, E. F. 2009, *ARA&A*, **47**, 427
 Hidaka, H., Watanabe, N., Shiraki, T., Nagaoka, A., & Kouchi, A. 2004, *ApJ*, **614**, 1124
 Hiraoka, K., Ohashi, N., Kihara, Y., et al. 1994, *CPL*, **229**, 408
 Hiraoka, K., Sato, T., Sato, S., et al. 2002, *ApJ*, **577**, 265
 Högbom, J. A. 1974, *A&AS*, **15**, 417
 Hogerheijde, M. R., Bergin, E. A., Brinch, C., et al. 2011, *Sci*, **334**, 338
 Huang, J., Andrews, S. M., Cleeves, L. I., et al. 2018, *ApJ*, **852**, 122
 Isella, A., Guidi, G., Testi, L., et al. 2016, *PhRvL*, **117**, 251101
 Kahane, C., Frerking, M. A., Langer, W. D., Encarnas, P., & Lucas, R. 1984, *A&A*, **137**, 211
 Kama, M., Bruderer, S., van Dishoeck, E. F., et al. 2016, *A&A*, **592**, A83
 Kastner, J. H., Qi, C., Dickson-Vandervelde, D. A., et al. 2018, *ApJ*, **863**, 106
 Limbach, H.-H., Buntkowski, G., Matthes, J., et al. 2006, *ChemPhysChem*, **7**, 551
 Loomis, R. A., Cleeves, L. I., Öberg, K. I., et al. 2018, *ApJ*, **859**, 131
 Loomis, R. A., Cleeves, L. I., Öberg, K. I., Guzman, V. V., & Andrews, S. M. 2015, *ApJL*, **809**, L25
 Loomis, R. A., Öberg, K. I., Andrews, S. M., & MacGregor, M. A. 2017, *ApJ*, **840**, 23
 McMullin, J. P., Waters, B., Schiebel, D., Young, W., & Golap, K. 2007, in *ASP Conf. Ser. 376, Astronomical Data Analysis Software and Systems XVI*, ed. R. A. Shaw, F. Hill, & D. J. Bell (San Francisco, CA: ASP), 127
 Noble, J. A., Theule, P., Mispelaer, F., et al. 2012, *A&A*, **543**, A5
 Öberg, K. I., Guzmán, V. V., Merchantz, C. J., et al. 2017, *ApJ*, **839**, 43
 Pegues, J., Öberg, K. I., Bergner, J. B., et al. 2020, *ApJ*, **890**, 142
 Podio, L., Bacciotti, F., Fedele, D., et al. 2019, *A&A*, **623**, L6
 Podio, L., Garufi, A., Codella, C., et al. 2020, arXiv:2008.12648
 Qi, C., Öberg, K. I., & Wilner, D. J. 2013, *ApJ*, **765**, 34
 Salinas, V. N., Hogerheijde, M. R., Mathews, G. S., et al. 2017, *A&A*, **606**, A125
 Schöier, F. L., van der Tak, F. F. S., van Dishoeck, E. F., & Black, J. H. 2005, *A&A*, **432**, 369
 Schwarz, K. R., Bergin, E. A., Cleeves, L. I., et al. 2016, *ApJ*, **823**, 91
 Teague, R. 2019, *JOSS*, **4**, 1632
 Teague, R., Henning, T., Guilloteau, S., et al. 2018, *ApJ*, **864**, 133
 Teague, R., & Loomis, R. 2020, *ApJ*, **899**, 157
 Testi, L., Birmstiel, T., Ricci, L., et al. 2014, in *Protostars and Planets VI*, ed. H. Beuther et al. (Tucson, AZ: Univ. Arizona Press), 339
 Thi, W. F., van Zadelhoff, G. J., & van Dishoeck, E. F. 2004, *A&A*, **425**, 955
 Tudorie, M., Cacciani, P., Cosléou, J., et al. 2006, *A&A*, **453**, 755
 van der Marel, N., van Dishoeck, E. F., Bruderer, S., & van Kempen, T. A. 2014, *A&A*, **563**, A113
 van Zadelhoff, G. J., Aikawa, Y., Hogerheijde, M. R., & van Dishoeck, E. F. 2003, *A&A*, **397**, 789
 van't Hoff, M. L. R., Harsono, D., Tobin, J. J., et al. 2020, *ApJ*, **901**, 166
 van't Hoff, M. L. R., Tobin, J. J., Harsono, D., & van Dishoeck, E. F. 2018, *A&A*, **615**, A83
 van't Hoff, M. L. R., Walsh, C., Kama, M., Facchini, S., & van Dishoeck, E. F. 2017, *A&A*, **599**, A101
 Visser, R., Doty, S. D., & van Dishoeck, E. F. 2011, *A&A*, **534**, A132
 Walsh, C., Loomis, R. A., Öberg, K. I., et al. 2016, *ApJL*, **823**, L10
 Walsh, C., Millar, T. J., Nomura, H., et al. 2014, *A&A*, **563**, A33
 Wang, Y., Tennyson, J., & Yurchenko, S. N. 2020, *Atoms*, **8**, 7
 Watanabe, N., & Kouchi, A. 2002, *ApJL*, **571**, L173
 Watanabe, N., Nagaoka, A., Shiraki, T., & Kouchi, A. 2004, *ApJ*, **616**, 638
 Zhang, K., Bergin, E. A., Blake, G. A., Cleeves, L. I., & Schwarz, K. R. 2017, *NatAs*, **1**, 0130